Redox mechanisms and metal fluoride stability in alkali fluoride corrosion -confirmed by experiment

Corrosion Science 260 (2026) 113538

Contents lists available at ScienceDirect

Corrosion Science

journal homepage: www.elsevier.com/locate/corsci

Redox mechanisms and metal fluoride stability in alkali fluoride corrosion -confirmed by experiment

Aida Nikbakht [a,*], Per Malmberg [a], Behnam Bahramian [b], Christine Geers [a]

[a] Department of Chemistry and Chemical Engineering, Chalmers University of Technology, Gothenburg 41296, Sweden
[b] Battery Cathode Materials, Umicore, Olen, B-2250, Belgium

ARTICLE INFO

Keywords:
Metal fluorides
Alternative to active oxidation
Alkali fluorides
Redox
Flux transport mechanism
Inconel 625

ABSTRACT

The corrosion behavior of Inconel 625 in contact with LiF was compared with its behavior in NaF at 600°C in air. Thermodynamic calculations were carried out to determine the stability of metal fluorides in both conditions, confirming salt specific element depletion. TOF-SIMS was conducted to examine the lithium-ion behavior in the oxide and metal over short-term and long-term exposures. A redox mechanism is suggested where fluoride ion A redox mechanism is suggested where fluoride ion ingress into the alloy towards an inner anode is discussed coupled with an outer anode at the alloy surface. The diffusion of lithium ions is considered a passive process along cation diffusion paths. The suggested mechanism discusses also why the presence of fluorine gas in the corrosion process is not viable. The presented mechanism and energetic pathway are in full agreement with the experimental observations and can be easily transferred to other alkali fluoride experiments in literature.

1. Introduction

Alkali fluoride salts are integral to a range of industrial processes, particularly in nuclear reactors, thermal storage, battery production and recycling. When it comes to salt melts as coolants for nuclear reactors, usually a mixture of alkali fluorides is considered for so-called fluoride-cooled high temperature reactors (FHR) [1]. Due to the fluorides' low vapor pressure, high thermal stability, and turbulent heat-transfer metrics, the FLiNaK eutectic melt has outperformed other mixtures [2]. In contrast to salt-free high temperature oxidation, where a protective alumina or chromia scale can grow slowly, no sufficiently stable scale forms in the presence of mixed alkali and halogenide ions. As a result, the corrosion process is controlled by the intermediate formation of metal fluorides [3,4].

In 1987 the National Aeronautics and Space Administration (NASA) conducted a study in which equilibrium concentrations of different metal fluorides were calculated for the respective metal (M) in contact to LiF, NaF and KF separately [5]. Based on this study, the tendency of different metals (M) for forming their corresponding metal fluorides showed the same order in all three salts, increasing in the following order: Ni<Co<Fe<Cr<Al. This study was initially performed in a supposedly inert atmosphere. In a later section of the report, the role of water impurity was also examined and discussed. It was found that water contributed to HF formation, hydrogen ion reduction, and metal oxide formation. Fluorine gas was never discussed to be generated in this report and hydrogen protons was mentioned to be reduced [5].

In this study from NASA, the heat of formation for different metal fluorides from their respective reaction of metal and fluorine gas has not been used explicitly. However, in 2009 Olson et al. [6] used heat of formation enthalpies, independent of the specific fluoride salt to reason the aggressivity of fluorides salts on metals. In the study by Olson et al., fluorine gas (F_2) has been implemented into the thermodynamic considerations, although fluorine has not been actively injected to the system [6]. As a result of implementing F_2 into the reactions with metals, all metal fluorides are reported to be forming spontaneously. Other studies have also referred to these calculations regarding the stability and formation of metal fluorides [3,7–12], regardless of the alkali fluoride salt which has been used.

A comparison between these two studies shows that NASA's results [5] did not require F_2 and that Olson et al.'s assumptions of presence of fluorine gas (F_2) might overestimate the corrosivity of the salt. In addition, the role of water impurity was not discussed in the study by Olson et al. [6]. Though, despite the different redox reactions, the tendency for the formation of different metal fluorides was close to the order reported from NASA [5].

In order to study the formation of FeF_3 from fluorine gas, Zhou and

* Corresponding author.
E-mail address: nikbakht@chalmers.se (A. Nikbakht).

https://doi.org/10.1016/j.corsci.2025.113538
Received 28 April 2025; Received in revised form 21 November 2025; Accepted 7 December 2025
Available online 8 December 2025

Johnson et al. actively injected fluorine gas into the system, where they could reasonably include F_2 into the thermodynamic calculations [13,14]. However, when fluorine gas is not actively injected, the formation of fluorine gas from alkali fluorides in contact to oxygen or metal oxides can only be speculated.

Many studies have examined corrosion in alkali fluoride salts under an inert atmosphere, often referencing the enthalpy of formation of metal fluorides despite the absence of fluorine gas injection into their systems and not considering possible redox-active impurities [3,7–12]. However, also under oxidizing conditions, some studies have attributed corrosion by alkali fluoride salts to intermediate, recirculating fluorine gas formation [15,16]. These studies base their discussions on a mechanism, commonly referred to as "active oxidation" which was first proposed by Grabke et al. [17]. Active oxidation in the case of fluoride salts proposes the formation of fluorine gas from the reaction between condensed alkali fluorides and the oxide scale on the metal. In humid conditions, the possibility of the formation of HF (g) is considered, which can become oxidized and lead to the formation of fluorine gas and water. Gaseous fluorine is then considered to reach the metal/oxide interface through the cracks of the oxide scale and react with the alloy to form metal fluorides, which in turn undergoes oxidation. This mechanism has been mostly studied in case of chloride salts [18,19] but applied to alkali fluoride salt corrosion as well [16].

Since fluorine gas is typically not injected into alkali salts during corrosion experiments, this study will provide an alternative mechanism. It is as well examined why the so-called "active oxidation" mechanism which requires molecular fluorine as transient product, is not applicable to fluoride salt corrosion under oxidizing conditions. In this context, oxidizing conditions refer to environments ranging from air exposure to the presence of oxygen impurities. Provided that all water and oxygen impurities are entirely removed, molten alkali fluoride salts lack a sufficient thermodynamic driving force to corrode alloys. Thus, under such conditions, pure fluoride salts remain chemically non-reactive with the alloy constituents [9,20,21]. However, in a study attempting to remove impurities in the salt FLiBe by injecting HF and H_2, it was shown that 180 ppm of trace HF remained dissolved in the salt [22]. This amount remained constant in the study by Kondo et al., which would mean that HF was generated during the exposure as well. Also in the study by Olson et al., trace impurities are expected to have a significant role in corrosion, though allegedly, not the focus of that study [6]. Considering the significant role of oxygen and water, either as an impurity or in an oxidizing atmosphere, we propose an alternative redox mechanism that does not require fluoride oxidation. In this model, oxygen is reduced by metals, while alkali ions and fluoride retain their oxidation states at any stage of the suggested mechanism and rather act as charge compensation and fluxing agents.

We found no calculation in literature, for the formation of metal fluorides in the metal that exclude fluorine gas in the reaction. Since we came to an alternative redox path, it was found necessary to recalculate these Gibbs energy values reported from literature [6] which consider the presence of fluorine gas (F_2) in the salt systems. In this study, we calculate the Gibbs free energy of formation for different metal fluorides based on the alkali fluoride salt and the presence of an oxidant, here oxygen. Although neither the alkali metal nor the fluoride component change oxidation state in our suggested mechanism, the stability of the metal fluoride is dependent on the salt used and in turn the corresponding alkali oxide stability.

This study compares the corrosion behavior of Inconel 625 in contact with lithium fluoride (LiF) and sodium fluoride (NaF) salts at 600°C in air. LiF and NaF were selected to test the salt-specific nature of metal fluoride stability and to validate the proposed inner-anode/outer-cathode redox mechanism. By substituting Li with Na while keeping all other variables identical, we show that intergranular attack occurs only in LiF for elements in alloy 625 at 600 °C. Calculations built on the suggested mechanism of metal fluorides formation reveal a striking contrast: while no metal fluorides are stable in NaF, certain metal fluorides (CrF_2, CrF_3, FeF_2, and NbF_5) tend to form in LiF. The findings are in line with the experimental data and support the proposed mechanism, which excludes fluorine gas involvement.

The alloy microstructure and the oxide scale were analyzed using scanning electron microscopy (SEM) and the corrosion products were analyzed using X-ray diffraction (XRD). Since lithium comprised the cationic species in LiF, time of flight secondary ion mass spectroscopy (TOF-SIMS) was used to detect any possible involvement of lithium in the corrosion attack.

2. Experimental

2.1. Sample preparation and exposure

Lithium fluoride (LiF, 97 %) and sodium fluoride (NaF, 99 %) were purchased from Thermo Scientific. Inconel 625 sheet was selected for this study and was purchased from ThyssenKrupp VDM with the trademark NICROFER 6020 HMQ. The plate was hot rolled and heat treated at 1020 °C. The nominal composition of this alloy can be found in Table 1. Inconel 625 strips ($350 \times 10 \times 3\ mm^3$) were cut and polished to a 600-grit finish using a silicon carbide grinding band.

Two metallic strips were individually immersed in molten LiF and NaF salts, each contained within a long alumina crucible, as illustrated in Fig. 1. The alumina crucibles measured 500 mm in length and had an inner diameter of 12 mm, providing an approximate 2 mm clearance around the samples to ensure complete and uniform exposure to the alkali fluoride salts.

The crucibles were housed inside a stainless-steel vessel placed within a vertical furnace configuration. This setup was specifically designed to maintain a controlled temperature gradient along the length of the crucibles, ranging from approximately 600 °C at the bottom to 50 °C at the top. The temperature profile was calibrated to simulate realistic thermal conditions experienced during salt corrosion processes. Filtered, dry air was continuously introduced through a gas inlet at the top of each crucible.

It is important to note that even at the hottest section of the strip (600°C), where corrosion analysis was conducted, the exposure temperature remained well below the melting points of LiF (848°C) and NaF (993°C). In order not to affect the chemistry of the samples, no post-exposure washing was performed before analysis.

2.2. Analytical techniques

To characterize the samples, the hottest section of each strip was cut into a $10 \times 10 \times 3\ mm^3$ coupon using a low-speed diamond saw without coolant. A water-free lubricant (Lubricant Yellow) was used during post-exposure sample preparation for microstructural analysis.

Surface investigations were performed using scanning electron microscopy (SEM) in backscattered electron (BSE) mode at an acceleration voltage of 15 kV. Both imaging and elemental analysis were conducted with a JEOL JSM-7800F Prime SEM, equipped with an energy-dispersive spectroscopy (EDS) detector.

The crystalline phases of the corrosion products were identified using X-ray diffraction (XRD) analysis. This was carried out with a Bruker D8 Discovery diffractometer, equipped with a Cu source, over a 2θ range of 10°–90°.

The lithium ingress in samples exposed to LiF was analyzed using a TOF-SIMS V instrument (ION-TOF, GmbH, Münster, Germany) with the following setting for the ion beam: Bi_3^+ , 0.45pA for the spectrometry mode and 0.6 pA for the fast-imaging mode. The acceleration voltage

Table 1
Nominal alloy compositions (wt%) of the Inconel 625 provided by the supplier.

Ni	Cr	Mo	Fe	Nb	Ti	Si	Others
balance	21.51	8.69	4.32	3.31	0.20	0.12	C 0.02

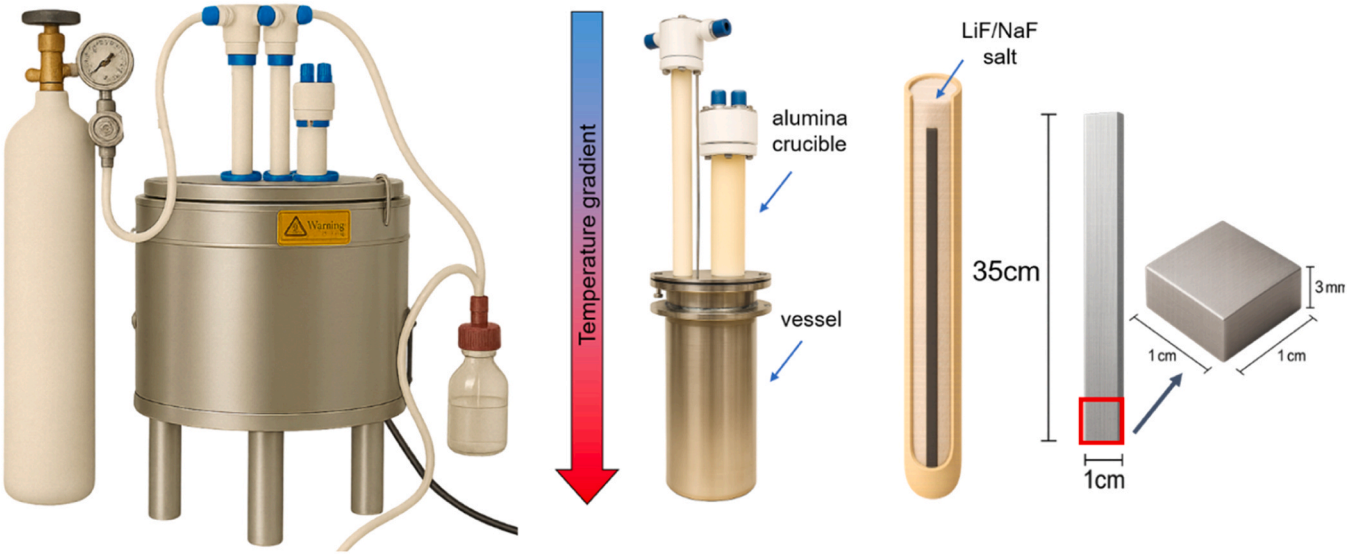

Fig. 1. vertical setup, used to expose samples to LiF and NaF.

was set at 30 keV with a focus of approximately 100 nm. The mass resolution was nominal in fast imaging mode and the average primary ion dose was 8.11×10^{12} ions/cm^2. Image analysis was performed using the Surface Lab 7 software (Version 7.4, ION-TOF, GmbH, Münster, Germany).

The spectrometry mode of the instrument was used to understand and assign the peaks clearly. The delayed extraction mode can lead to better mass resolution in general, though, a light ion like lithium can be underreported in this mode. Hence, the fast-imaging mode was used, where higher image resolution is also offered [23]. The low-resolution mass spectra which is a result of the high image resolution mode was not problematic in this case, since the lithium-ion mass (m/z 7.13) was not overlapping with any other species. In order to detect both lithium and fluoride ions, the analysis was carried out for both electropositive and electronegative ions. The sample which was exposed for only 168 h was sputtered with oxygen and cesium ions in positive and negative polarity respectively with the ion dose of 9.2×10^{14} ions/cm^2. In the longer exposure (after 1000 h), lithium and fluoride ingress were possible to be detected without sputtering.

3. Results

Cross section images and EDS results for Inconel 625 after 1000 h of exposure at 600°C in LiF and NaF will be presented in the following two sections. Based on the results, Inconel 625 shows very different corrosion attack in contact to these two salts even though the experimental procedure was identical except for the cationic species of the used salt.

3.1. LiF exposure

Fig. 2 shows a backscatter electron image together with the EDX element maps for the alloy cross section after 1000 h of exposure to LiF.

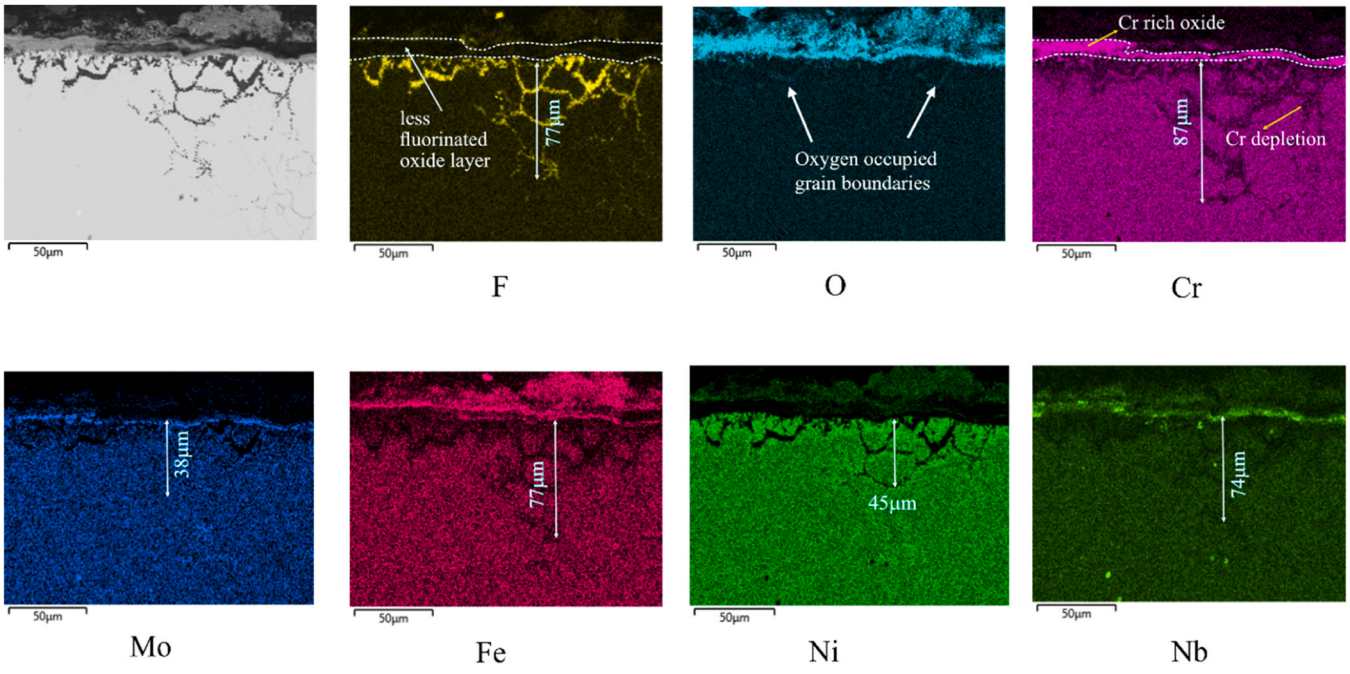

Fig. 2. SEM and EDX image of Inconel 625 sample cross-section after 1000 h exposure in LiF salt and air at 600 °C.

EDX maps in Fig. 2 show that fluoride has entered the microstructure of Inconel 625 and reached a depth of 77 μm into the alloy. During the shorter exposures (168 h) which have not been included in the current study, oxygen did not penetrate the alloy microstructure and always stayed on top of the metal. Also in Fig. 2, after 1000 h, oxygen was only found at very wide grain boundaries filled with fluoride close to the metal oxide interface. EDX maps show depletion for Cr, Fe and Nb from the grain boundaries where fluoride has penetrated. These alloying elements have been depleted to different extents. After 1000 h of exposure, Cr shows continuous 87 μm of depletion depth which is deeper than Fe and Nb. The difference in the depth of depletion for different alloying elements indicates selective depletion. Fluoride enrichment was seen in the outer part of the oxide scale which is rich in Fe and Ni, but not in the lower part which is rich in Cr. The SEM image shows that the outer Fe and Ni rich oxide scale was more defect rich and less compact in comparison with the inner oxide scale.

Since it is not possible to detect lithium through the EDX detector, TOF-SIMS analysis was conducted to see the behavior of lithium in the corrosion attack by LiF. Samples exposed for 168 h and 1000 h were both analyzed via TOF-SIMS to see if lithium behavior changes over time. Lithium and fluoride have to be detected in two different polarities (positive and negative polarity respectively) in TOF-SIMS. Hence, the areas in which chromium and lithium have been detected are slightly shifted from the area where the fluoride map was taken.

Fig. 3 shows TOF-SIMS results after exposure to LiF for 168 h. As can be seen in Fig. 3, fluoride has diffused into the grain boundaries of the metal. Fluoride enrichment in the grain boundaries of the alloy after 168 h exposure was detected via EDS in our previous study as well [24]. If lithium diffuses into the alloy and is to be detected, it would be at the grain boundaries of the alloy. However, the lithium map in Fig. 3 showed the presence of lithium ion only in the pores at the metal oxide interface. It is noteworthy that underneath the pores at the metal/oxide interface after 168 h also some lithium signals at noise level were detected. This was only at noise level and most likely due to the sample preparation where lithium from the interface was smeared not only in the grain boundaries but also on the grains. This is while the TOF-SIMS analysis in negative mode revealed the penetration of fluoride deeper into the grain boundaries up to 16 μm. TOF-SIMS results both after 168 h and 1000 h show lithium enrichment also in the oxide/salt interface. However, no fluoride enrichment is seen at the oxide/salt interface neither after 168 h nor 100 h of exposure. These observations underline the fact that lithium and fluoride do not diffuse into the grain boundaries together and it is only fluoride which diffuses along the metal grain boundaries after 168 h.

In order to see if the behavior of lithium-ion changes over longer exposures, TOF-SIMS analysis was carried out after 1000 h too. Results in Fig. 3, after 1000 h of exposure, showed the penetration of lithium into the upper grain boundaries close to the metal oxide interface up to 56 μm. Fluoride has diffused the grain boundaries of the alloy significantly deeper than lithium. The maps show the penetration of lithium up to 56 μm where it stops. However, fluoride penetration continues to at least 74 μm and does not stop. This confirmed the fact that lithium and fluoride separate before diffusing into the grain boundaries and do not diffuse together. TOF-SIMS results in Fig. 3, show both Cr depletion in

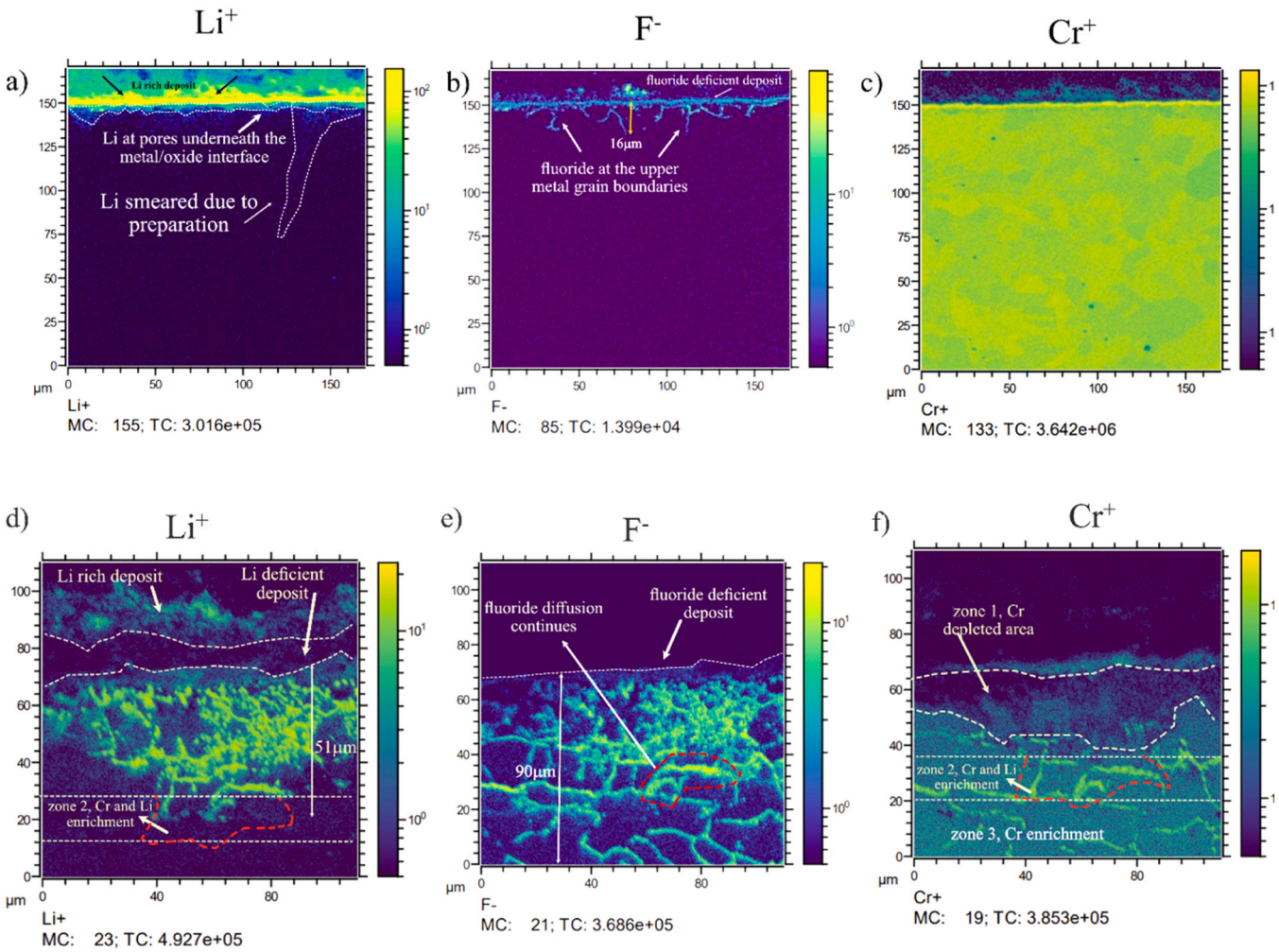

Fig. 3. TOF-SIMS analysis on samples exposed to LiF a, b, c) after 168 h d, e, f) after 1000 h in logarithmic scale.

the upper grain boundaries and Cr enrichment underneath. Lithium enrichment was mostly detected in the upper grain boundaries where Cr was depleted.

3.2. NaF exposure

Inconel 625 behaved very differently in contact with NaF. Significant oxide spallation was observed during NaF exposure after both 168 h and 1000 h. After 1000 h of exposure, one-third of the sample thickness (1 mm) was lost due to corrosion, excluding the contribution of the spalled oxide layer. This thickness loss corresponds to an estimated mass loss of approximately 263 mg/cm^2, which makes NaF by far a much more corrosive medium than LiF. The thickness of the oxide scale in Fig. 4 shows 123 μm which is only the remnant of the non-adhesive oxide scale after spallation. As can be seen in Fig. 4, there was no intergranular attack seen in Inconel 625 even after 1000 h of exposure. Sodium and fluoride were found at the same spots in the oxide scale, though never detected as a part of the oxide phases in XRD. The oxide scale shows two different morphologies in Fig. 4. The lower part of the oxide scale is rich in Mo, Na and fluoride and the upper part with a more granular oxide structure where Cr, Fe and Ni participate. The Mo rich layer shows a layered and compact structure. The upper part of the oxide scale consists of Fe, Nb and Cr rich islands, spread in a porous sodium and fluoride rich matrix. These sodium fluoride enrichments do not overlap with metal enrichments, meaning that the salt components do not form an oxide phase together with the metal cations.

Since there was a Mo rich scale seen at the lower part of the oxide scale at lower magnification in Fig. 4, it was interesting to see the lower part at higher magnifications. Fig. 5 shows the lower part of the oxide scale at a higher magnification. As can be seen in Fig. 5, there is a sodium and fluoride rich layer adjacent to the metal, where the Mo rich oxide scale has not started. On top of this layer there is another layer which is rich in molybdenum, oxygen, sodium and less rich in fluoride. Higher magnifications of the oxide scale showed Cr and Fe enrichment in the upper parts of the oxide scale. The rapid oxidation resulted in the porous structure of the upper oxide scale, which is rich in Fe and Cr. No overlap between sodium and metal oxides was seen in EDS and no sodium chromates or sodium iron oxide were detected in XRD.

Fig. 6 shows the XRD analysis which was conducted on both NaF and LiF exposed samples in order to identify different phases in the oxide scale. In NaF exposures, the oxide scale was identified as primarily nickel oxide with additional Cr-Ni- and Fe-Ni spinels. Considering the fact that the oxide scale was 123 μm thick, the most intense diffraction signals are from the oxide scale and not the underlying metal. These signals with the highest intensity in the diffraction pattern were close to both $Cr_{0.3}Ni_{0.7}O_{0.65}$ (see comments for this phase in the Appendix) and NiO. Also, EDX maps showed overlapping enrichment of Cr and Ni in the oxide, which confirms the formation of $Cr_{0.3}Ni_{0.7}O_{0.65}$. This oxide has a rock salt structure where the cationic sites are shared by Ni (70 %) and Cr (30 %). EDS results showed enrichment for Na, Mo, O and F in the lower part of the oxide scale, also $Na_3MoO_3F_3$ was detected in XRD analysis which would represent the sodium molybdenum oxyfluoride layer at the metal/oxide interface. In addition, the XRD patterns for Na_3MoO_4F and $NaMoO_3F$ in literature show that these two compounds would have their most intense peak at 2θ= 27–28 ° [25,26]. In the diffractogram in Fig. 6a, there is a signal identified at 2θ= 27–28 ° which is assigned to $MoO_{2.8}F_{0.2}$.

4. Discussion

As mentioned in the results section, Inconel 625 showed different kinds of behavior in contact with LiF and NaF. Thermodynamic calculations in our previous study [24] confirmed that upon negative Gibbs reaction enthalpies for (R1), an outer cathode (reduction of oxygen) and inner anode reaction (cation formation along the alloy microstructure) allows for the inwards flux of fluoride ions to charge compensate cations at the inner anode and thereby forming metal fluorides.

$$\text{R1)}\quad M + nAF + \frac{n}{2}O_2 \rightarrow MF_n + \frac{n}{2}A_2O \quad (A = Li, Na), \quad M = \textit{transition metal}$$

These reactions between fluoride ions and selected alloying elements led to the formation of stable metal fluorides via intergranular attack [24]. Thermodynamic calculations in our previous study were in line with experimental results, showing that Cr, Fe and Nb are able to form stable metal fluorides at the grain boundaries of alloy 625. It is interesting to draw a comparison and do similar calculations in case of NaF exposures, since the cationic part of the salt has changed from Li to Na.

Reactions 1.1–1.9 in Table 2 show the corresponding calculations for different alloying elements in contact with NaF and oxygen at 600°C.

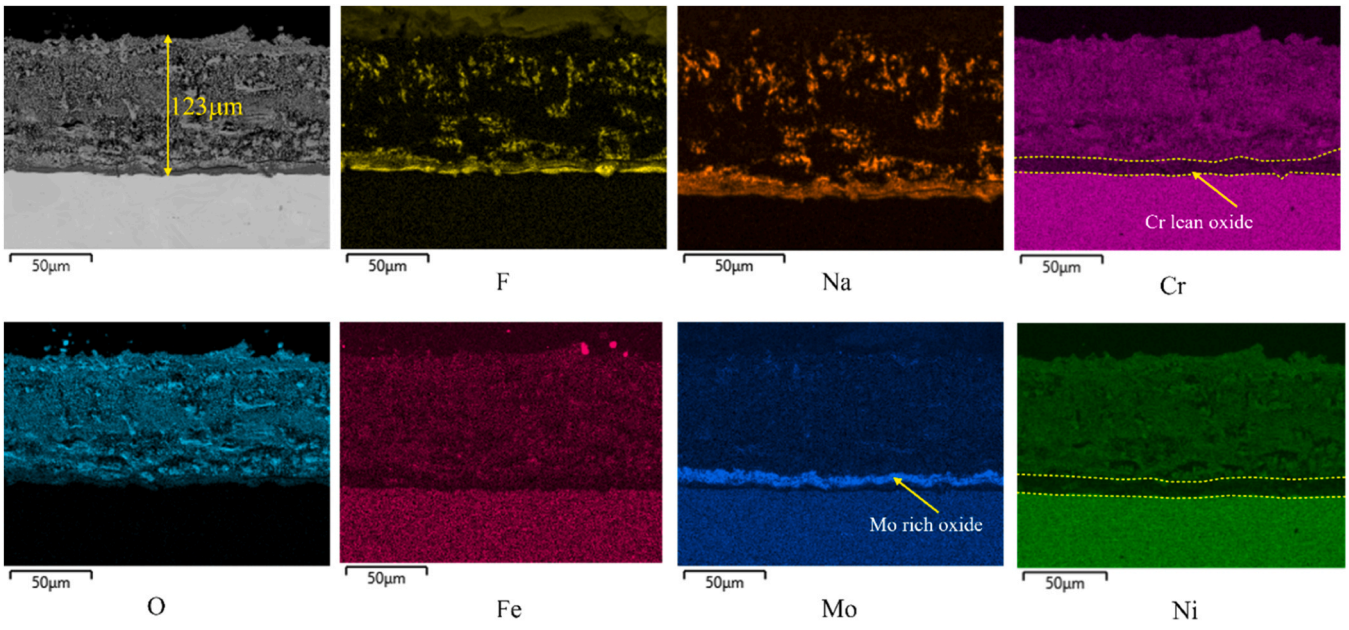

Fig. 4. EDX map of Inconel 625 exposed to NaF for 1000 h in oxidizing condition.

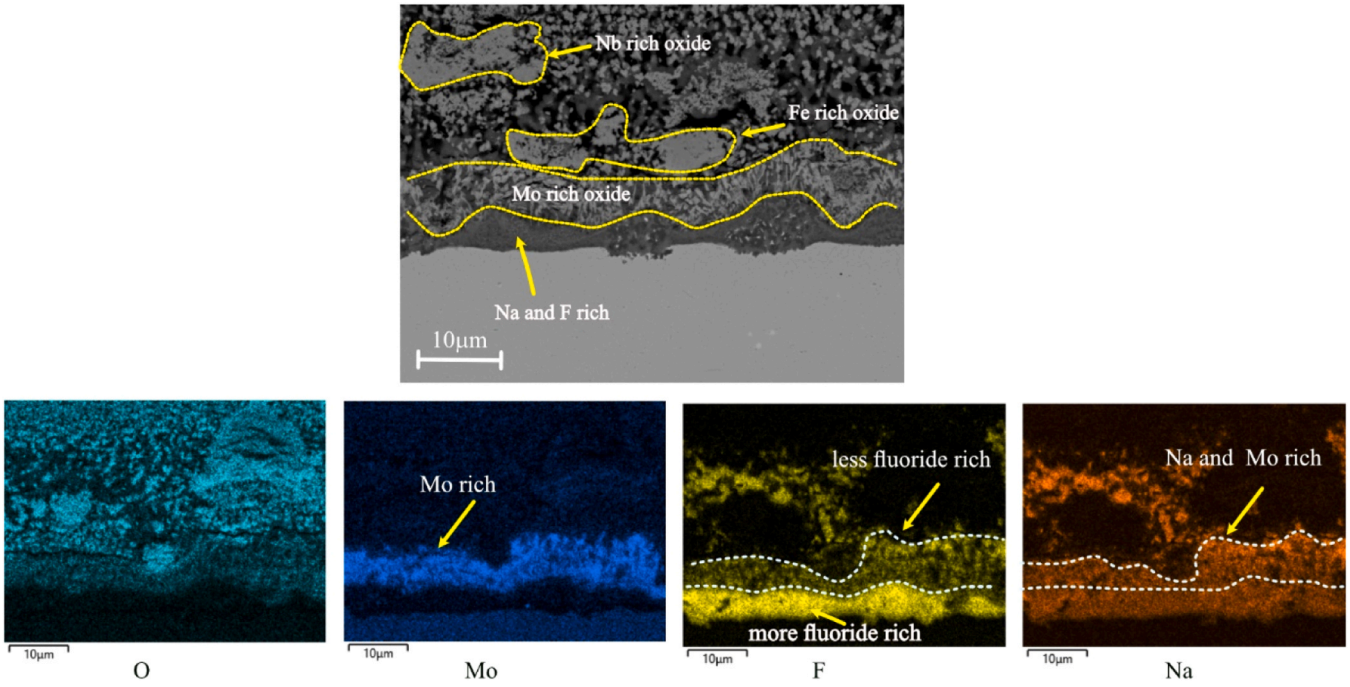

Fig. 5.) the lower part of the oxide scale in Inconel 625 sample exposed to NaF for 1000 h.

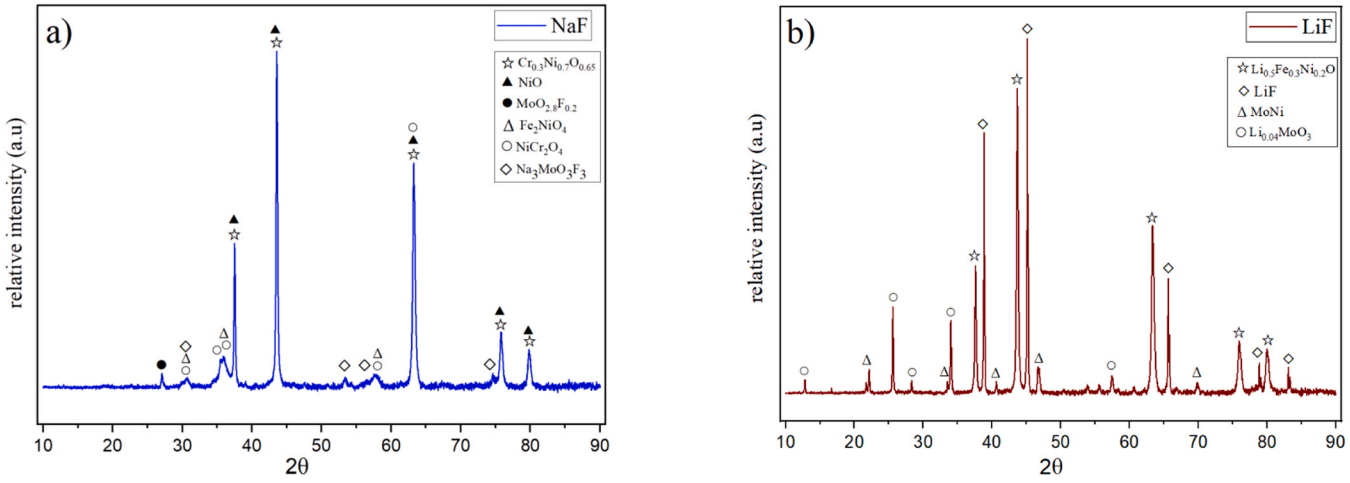

Fig. 6.) XRD patterns after 1000 h of exposure for a) NaF exposure b) LiF exposure at 600°C.

Table 2
Gibbs enthalpies retrieved from Factsage 7.3 [27] for relevant reactions for metal fluorides in NaF/O_2 environment.

No	*reaction*	*Reaction* $\Delta G^0_{600^\circ C}$ *in kJ*	compound
	Reactions at an inner anode and outer cathode		
*R*1.1	$Cr + 2NaF + 0.5O_2 \rightarrow CrF_2 + Na_2O$	+ 5	CrF_2
*R*1.2	$Cr + 3NaF + 0.75O_2 \rightarrow CrF_3 + 1.5Na_2O$	+ 45	CrF_3
*R*1.3	$Fe + 2NaF + 0.5O_2 \rightarrow FeF_2 + Na_2O$	+ 77	FeF_2
*R*1.4	$Fe + 3NaF + 0.75O_2 \rightarrow FeF_3 + 1.5Na_2O$	+ 161	FeF_3
*R*1.5	$Nb + 5NaF + 1.25O_2 \rightarrow NbF_5 + 2.5Na_2O$	+ 124	NbF_5
*R*1.6	$Ni + 2NaF + 0.5O_2 \rightarrow NiF_2 + Na_2O$	+ 149	NiF_2
*R*1.7	$Mo + 2NaF + 0.5O_2 \rightarrow MoF_2 + Na_2O$	+ 472	MoF_2
*R*1.8	$Mo + 3NaF + 0.75O_2 \rightarrow MoF_3 + 1.5Na_2O$	+ 432	MoF_3
*R*1.9	$Mo + 5NaF + 1.25O_2 \rightarrow MoF_5 + 2.5Na_2O$	+ 597	MoF_5

These results show the standard Gibbs free energy $\Delta G^\circ > 0$ for the formation of metal fluorides for every alloying element of Inconel 625 at 600°C, meaning that none of the transition metals among the alloying elements form stable metal fluorides in contact to NaF and oxygen. These thermodynamic calculations confirm the absence of any intergranular attack in EDS results from Inconel 625 exposed to NaF.

The ΔG° values calculated for the formation of different metal fluorides are illustrated in Fig. 7 for NaF (Table 2, R 1.1- R1.9) and LiF (R 4.1- R 4.9 in reference [24]). As summarized in Fig. 7b, CrF_2, CrF_3, FeF_2, and NbF_5 form spontaneously in contact with LiF at 600°C. This result was consistent with experimental observations which showed selective depletion of Fe, Cr, and Nb in the grain boundaries after 168 h of exposure to LiF in our previous study and Fig. 2 in the present study. This is while similar calculations presented in Fig. 7a for NaF at 600°C indicate that none of the metal fluorides fulfill the spontaneity condition ($\Delta G^{\circ} > 0$). Fig. 7 shows that even niobium, chromium, and divalent iron fluorides, which formed spontaneously in LiF exposures, show positive ΔG° values in NaF exposures. Considering that the calculations are based on R 1, it can be deduced that NaF is significantly more stable than the product, Na_2O.

These thermodynamic findings for NaF exposures are in line with SEM and EDX observations in Fig. 3, where no intergranular attack was detected, and fluoride diffusion into the alloy grain boundaries was absent. SEM images showed the formation of very defect rich and non-adherent oxides in NaF exposures which were not formed via diffusion-controlled kinetics through a scale but rather an ion flux through the salt coverage. This means a layer of unreacted NaF remains at the sample surface, acting as electrolyte flux, connecting the surface metal (anode), with the oxygen (cathode) over the salt. The absence of a distinct depletion zone for any of the alloy components, together with the very high material loss underlines that the corrosion kinetics are controlled by the fluxing process.

Reaction 1 represents how the reactions for the formation of different metal fluorides are suggested. If metal fluorides form spontaneously by reaction 1, an intergranular attack with fluoride enrichment in the grain boundaries would be possible too. As written in R1, the formation of transition metal fluorides is bound to fluoride release from the alkali fluoride salt and the formation of alkali oxide species (in this case Na_2O or Li_2O). If the alkali metal forms a stable alkali oxide, the released fluoride anions can activate the inner anode (metal cations) to form metal fluorides. Reactions 4.1–4.9 in case of LiF in our previous study [24] and NaF exposures (Table 2 in the present study) are written based on R1.

In case an intergranular attack is seen and metal cations are delivered to oxide ions through the formation of metal fluorides, the inner anode and outer cathode mechanism is valid. The inner anode is the metal component which is oxidized and oxygen which is being reduced forms the outer cathode. These reactions are written in the present form to represent the correct electron transfer and the formation of the corresponding products. As can be seen in R1.1-R1.9, neither the alkali metal nor the fluoride ion change oxidation state and always remain with their respective positive or negative charge.

Experimental results together with the thermodynamic calculations confirmed two different corrosion behaviors in LiF and NaF exposures. In the following section we will elaborate further on the mechanisms inferred by reaction 1 and discuss the two different processes.

4.1. LiF-driven corrosion mechanism

As stated in reaction 1, electron transfer occurs only between oxygen and the alloy metals. Fig. 8a illustrates the redox process for LiF exposures, showing that the overall reaction is the oxidation of the alloying metals by oxygen. In this process, oxygen is reduced by electrons originating from the alloy. At the site where these electrons are released (initially at the alloy surface and later within the microstructure at an inner anode) alloy metal cations are formed. These cations recombine with inward-diffusing, charge-compensating fluoride ions released from the salt. The remaining alkali ion at the surface is charge-compensated by the oxygen ion. This sequence implies that for every fluoride ion that enters the alloy microstructure, one positive charge must be created at the inner anode. This occurs through the reduction of oxygen at the surface.

This redox scenario needs to be energetically spontaneous to explain the intergranular attack. This is fulfilled for some of the alloy metals and thus fluoride ions can leave lithium cations and diffuse into the metal to form stable metal fluorides. By fluxing metal cations from deeper grain boundaries, fluoride ions accelerate the formation of metal oxides. As shown in Fig. 7b, by the formation of FeF_2, CrF_2, CrF_3 and NbF_5, their corresponding metal cations diffuse towards the metal/oxide interface. This is also visible in the oxygen EDS map in Fig. 2 after 1000 h of exposure, where oxygen ions have diffused into the upper grain boundaries to combine to the metal cations. Over time, fluoride ions diffuse deeper into the metal grain boundaries to charge compensate more metal cations and counter diffusing them up to the metal/oxide interface. This means that, in our suggested mechanism, fluoride enters the mechanism after leaving lithium in LiF salt. Hence fluoride is always in anionic form and once it diffuses into the metal, will not be transported back to the metal/oxide interface before all the Cr, Nb and Fe have been depleted in the alloy. In XRD measurements for LiF exposures in Fig. 6b, lithium metal oxides were detected, which means Li_2O and metal oxides have reacted and formed alkali metal oxides.

TOF-SIMS results after 168 h of exposure in LiF (Fig. 3a) also showed that lithium was absent in fluoride decorated grain boundaries. This was consistent with the understanding of the fluoride release from the alkali salt, while the alkali metal remains with oxide anions. This underlines the fact that lithium and fluoride do not diffuse together and separate before fluoride diffuses into the metal grain boundaries. As shown in Fig. 2, after 1000 h of exposure, most metal cations have already been depleted from the grain boundaries. After 1000 h TOF-SIMS results shown in Fig. 3d show that lithium is present in grain boundaries close to the alloy surface where chromium has completely been depleted. The comparison between 168 h and 1000 h confirmed that lithium does not start to diffuse through the grain boundaries together with fluoride. After long exposures, fluoride has reached deeper and depleted the grain boundaries from R1 accessible metals (Cr, Fe, Nb). The grain boundaries closer to the alloy surface have widened after 1000 h of exposure. At this stage, as illustrated in Fig. 8b, cation positions in the grain boundaries close to the metal/oxide interface, start to scramble with alloy metal and lithium cations. It can be concluded that in the upper grain boundaries which are depleted and are far from the lower Cr rich grain boundaries, lithium gets the chance to scramble and charge compensate for fluoride and eventually even oxygen in these widened grain boundaries, which is in agreement with a progressing oxide scale. This is in line with our suggested mechanism where lithium and fluoride separate, and fluoride diffuses into the metal grain boundaries singly. SIMS data in Fig. 3d,e and f show that fluoride diffusion into the metal is composed of three different regions: 1) The upper grain boundaries close to the metal/oxide interface where Cr has been depleted to a great extent 2) region 2 where simultaneous enrichments of Cr and Li cations are seen. Fluoride ions are charge compensated by both of the cations present at this region. 3) grain boundaries located deeper in the alloy where Cr has not been depleted yet and fluoride ions can be charge compensated only by specific alloying elements from the metal which form stable transition metal fluorides, meaning: Cr, Fe and Nb. Indeed, the presence of fluoride caused an intense chromium enrichment at these deep grain boundaries, defining the corrosion front. These distinct regions clarify that fluoride at the tip of the intergranular attack is charge compensated by already oxidized chromium ions. Oxidation happens by donating electrons to oxygen at the metal/oxide interface, and once the cations are formed, they can form intermediate metal fluorides which accelerate the transport and depletion of transition metals from the alloy to the oxide.

In another study where oxygen was reported to be an impurity also, TOF-SIMS depth profile confirmed the presence of lithium in nickel-base alloys [11]. According to our mechanism, the impurity oxygen is scrambling lithium into the metal in that study as well. Otherwise, there is no oxidizing agent for the alloying elements to oxidize and form metal fluorides.

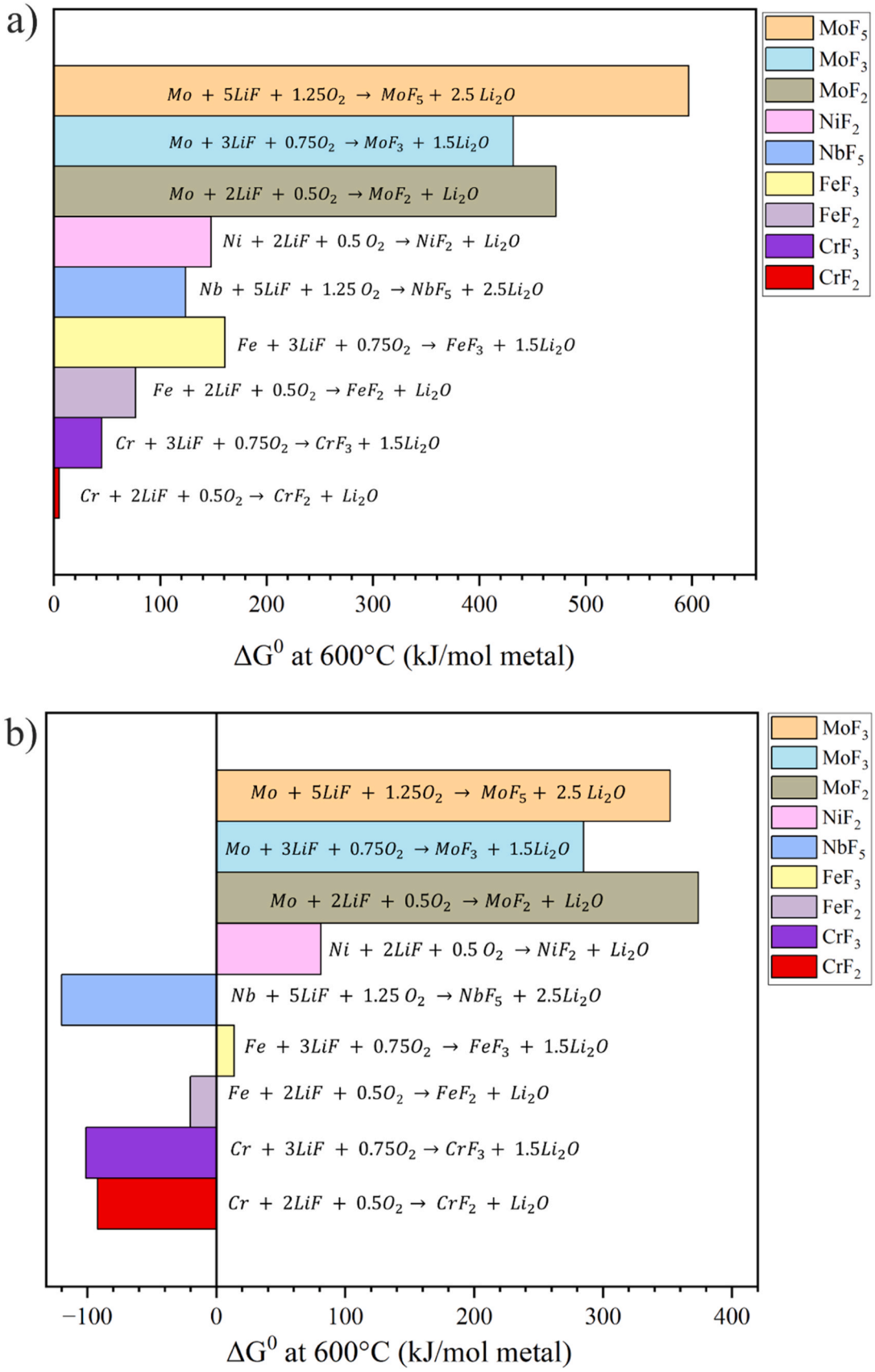

Fig. 7. Gibbs free reaction energies for different metals in contact to a) NaF b) LiF at 600°C.

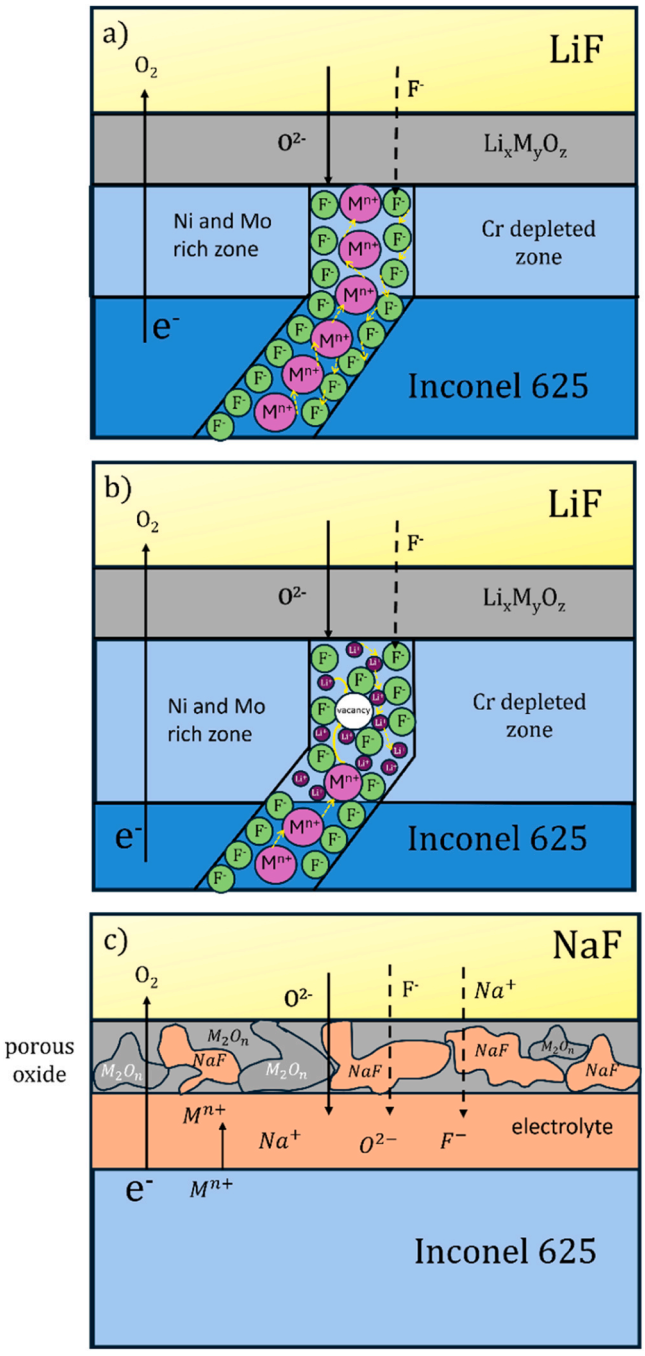

Fig. 8. Suggested diffusion paths for a) short LiF exposures b) long LiF exposures c) NaF exposures.

4.2. NaF-driven corrosion mechanism

A similar mechanism applies to NaF exposures as well. As shown in Fig. 8c, metal atoms which are in contact with NaF get oxidized and reduce oxygen atoms connected by the sodium fluoride electrolyte layer. This leads to the formation of a fluxing electrolyte at the metal/oxide interface, where sodium fluoride forms a flux with metal cations and oxygen anions. As shown in reaction 1, the formation of metal fluorides is bound to the stability of the corresponding alkali oxide. Sodium does not show stable oxide in these environments and the NaF compound remains as a vehicle for ionic transport on top of the metal. As a result, metal ions which are transported from the metal surface to reduced oxygen ions form a highly porous oxide on top of the fluxing electrolyte. This scenario is controlled by the ionic transport across the electrolyte.

The instability of metal fluorides in NaF exposures was already declared via calculations in reactions R1.1-R1.9 in Table 2 and presented schematically in Fig. 7a. Although the resultant metal fluorides are the same ones which form in LiF exposures, their formation is reliant on the stability of their corresponding alkali oxide. This implies that alkali and halogenide ions in sodium fluoride remain in a flux media, charge compensated at all times, but do not separate into their corresponding metal fluorides and alkali oxides (as observed for LiF). Therefore, no intergranular attack was observed in NaF as well as no element specific depletion. Hence, to discuss the formation and stability of metal fluorides from alkali halogenide salts, it is suggested to base the thermodynamic calculations on reaction 1.

4.3. Contrasting the described redox-process with the literature case

The presented results show that it is unnecessary and misleading to base the calculations for the formation of metal fluorides on F_2 gas molecules, because: First and most importantly, fluorine gas (F_2) has not been confirmed to exist in the system. In the coming section, it will be investigated and proven that it is not energetically plausible in this chemical surrounding to oxidize fluoride ions to fluorine (F_2) by oxygen. Secondly, calculations should be done for each alkali halogenide system separately, since the stability of the alkali oxide should also be taken into account.

In literature, the spontaneity of formation of metal fluorides has been calculated based on fluorine gas (F_2) [6]. We argue that F_2 as a gas molecule does not exist in our oxidation mechanism and fluoride ion remains negatively charged as F^-, which compensates for the metal cation charges. These metal cations are at the anode site which provides fluxing conditions towards the outer cathode, where oxide formation occurs. With this being said, several corrosion studies in fluoride salt, base the aggressive attack on spontaneous release of fluorine from the environment. We have explored a variety of suggested release scenarios for F_2 gas molecules and could not identify one which is energetically viable. Thus, corrosion by fluorides needs to be reasoned without the oxidation state of fluoride changing.

These studies refer to a mechanism entitled “active oxidation” which is based on the formation of F_2 as a gas molecule during the corrosion process. This mechanism suggests the initial formation of halogen gas molecules and that they remain in the system and act as a catalyst [17, 28]. In this framework, F_2 as a gas molecule is generated at the oxide/gas interface by oxidation of alkali fluorides or oxidation of HF by O_2. These fluorine gas molecules are then supposed to pass through the oxide and reach the metal/oxide interface to form metal fluorides while oxidizing the metal. These metal fluorides which are stable only at low oxygen partial pressures, are then presumed to be transported to the oxide/gas interface in gaseous form. Once these metal fluorides reach higher oxygen partial pressures at the oxide/gas interface, they are considered to form metal oxides and fluorine gas at the oxide/gas interface. As a result of this decomposition, fluorine gas will be released again and is claimed to penetrate towards the metal/oxide interface again, repeating the same cycle.

There are different arguments which challenge the theory of “active oxidation”, though, first we check the spontaneity of formation of F_2 as a gas molecule. We argue that corrosion in alkali fluorides does not thermodynamically involve the presence of F_2 in the environment. There are two sources suggested in the literature for the formation of halogen gas molecules. In the following we will explore and disprove suggested reactions with the environment as well with alloying elements to form metal fluorides.

Table 3
Gibbs enthalpies for reactions proposed for the so-called "active oxidation" theory, showing thermodynamic non-spontaneity.

No	*reaction*	*Reaction* $\Delta G^0_{800^\circ C}$ *in kJ*	*Reaction* $DG^0_{50^\circ C}$ *in kJ*
*R*3.1	$2NaF + Cr_2O_3 + 0.5O_2 \rightarrow 2NaCrO_2 + F_2$	+ 572	+ 618
*R*3.2	$2NaF + Fe_2O_3 + 0.5O_2 \rightarrow 2NaFeO_2 + F_2$	+ 509	+ 551
*R*3.3	$2LiF + Fe_2O_3 + 0.5O_2 \rightarrow 2LiFeO_2 + F_2$	+ 459	+ 521
*R*4.1	$4NaF + Cr_2O_3 + 2.5O_2 \rightarrow 2Na_2CrO_4 + 2F_2$	+ 774	+ 758
*R*4.2	$4LiF + Cr_2O_3 + 2.5O_2 \rightarrow 2Li_2CrO_4 + 2F_2$	+ 805	+ 815
*R*5.1	$2LiF + \frac{1}{2}O_2 \rightarrow Li_2O + F_2$	+ 618	+ 975
*R*5.2	$2NaF + \frac{1}{2}O_2 \rightarrow Na_2O + F_2$	+ 709	+ 657

4.4. The oxidation of HF as a gas and formation of fluorine gas molecules and water

R2) $2HF(g) + \frac{1}{2}O_2(g) \rightarrow F_2(g) + H_2O(g)$

$\Delta G^0_{50^\circ C} = +316kJ \qquad \Delta G^0_{800^\circ C} = +368kJ$

1) Another proposed source of fluorine gas formation involves the reaction of condensed halides with oxygen, with or without the participation of an oxide scale. If we consider A as an alkali metal, X as a halogen, and M as iron or chromium, the possible reactions would be:

R3) $2AX + M_2O_3 + \frac{1}{2}O_2 \rightarrow 2AMO_2 + X_2 \quad (A = Li, Na), M = transitionmetal$

R4) $2AX + M_2O_3 + \frac{1}{2}O_2 \rightarrow 2A_2MO_4 + X_2 \quad (A = Li, Na), M = transitionmetal$

R5) $2AX + \frac{1}{2}O_2 \rightarrow A_2O + X_2 \quad (A = Li, Na)$

We can now check if formation of fluorine gas is energetically plausible through any of these reactions in both NaF and LiF experiments. Table 3 shows the thermodynamic calculations for the stability of fluorine gas in these environments.

As shown in Table 3, the generation of fluorine gas is not energetically favored through any of the reactions (R3.1-R5.2) which are considered as possibilities in the theory of active oxidation. In all of these reactions (R3.1-R5.2) fluoride is being oxidized, changing oxidation state from −1–0, while oxygen is being reduced, changing oxidation state from 0 to −2. Fluorine is the most electronegative element and the strongest oxidizer which readily combines with most organic and inorganic materials [29]. Hence, oxidizing fluoride (F^-) does not happen spontaneously upon reacting to oxygen gas.

After this exercise, it can be concluded that the involvement of molecular fluorine is neither thermodynamically explainable nor necessary for the observed corrosion attack, since there is a thermodynamically sound alternative reaction path in the first part of the discussion section and all observations can be related and reasoned by Reaction 1.

5. Conclusion

Basing our studies on an outer cathode inner anode redox mechanism, the corrosion mechanism driven by LiF was distinguished from NaF, by the energetically inaccessible inner anode for te latter. This study demonstrates intergranular attack for the corrosion attack in the presence of LiF, while no such attack was detected in contact with NaF. Thermodynamic calculations for the formation of metal fluorides in the presence of NaF and air, showed positive Gibbs free reaction energies for all alloying elements, consistent with the experimental observations. In contrast, calculations for LiF revealed negative Gibbs free reaction energy values for the formation of CrF_2, CrF_3, FeF_2, and NbF_5, which aligns with the intergranular depletion of Cr, Nb, and Fe. Noteworthy, chromium fluoride was detected at the innermost intergranular attack via SIMS.

Furthermore, previous literature has thermodynamically investigated metal fluoride formation by considering the reaction of metals with fluorine gas. However, in this study, we propose an alternative for calculating Gibbs free energies for the underlying corrosion reactions. In the suggested approach, the cathodic oxygen reduction reaction and the anodic oxidation of the metal components are not necessarily at the same location. We further discuss why the inclusion of fluorine gas in the reaction model is unnecessary for our system and explain why the "active oxidation" theory cannot be applied in this case.

CRediT authorship contribution statement

Christine Geers: Writing – review & editing, Visualization, Validation, Supervision, Project administration, Funding acquisition, Data curation, Conceptualization. **Behnam Bahramian:** Writing – review & editing. **Per Malmberg:** Writing – review & editing, Validation, Methodology, Formal analysis. **Aida Nikbakht:** Writing – original draft, Visualization, Investigation, Formal analysis, Data curation.

Declaration of Competing Interest

The authors declare the following financial interests/personal relationships which may be considered as potential competing interests: Christine Geers reports financial support was provided by Umicore. If there are other authors, they declare that they have no known competing financial interests or personal relationships that could have appeared to influence the work reported in this paper.

Acknowledgements

We want to thank Umicore, Belgium, for the financial support of this undertaking. Furthermore, we would like the head of our mechanical workshop Torbjörn Jönsson for evermore finding technical solutions for operating these challenging experiments.

Appendix

Extended XRD discussion

In NaF exposures the oxide scale was nickel rich with Cr and Fe. Considering the fact that the oxide scale was at least 120 μm thick, the most intense peaks in the diffraction pattern were from the oxide scale and not the underlying metal. These peaks with the highest intensity in the diffraction

pattern were close to both $Cr_{0.3}Ni_{0.7}O_{0.65}$ and NiO. However, $Cr_{0.3}Ni_{0.7}O_{0.65}$ which has the pdf number 04–011–9040 was deleted from the database but showed better match compared to NiO with most of the intense signals in the diffraction pattern. Table 3 shows the 2θ values for the three peaks with the highest intensity for both NiO and $Cr_{0.3}Ni_{0.7}O_{0.65}$ together with the experimental data collected. The values for 2θ extracted from the XRD pattern in our NaF experiment are closer to the ones in $Cr_{0.3}Ni_{0.7}O_{0.65}$ in case of all three peaks. Also, EDX maps showed that enrichment of Cr and Ni was never standing out alone. $Cr_{0.3}Ni_{0.7}O_{0.65}$ has a rock salt structure where the cationic sites are shared by Ni (70 %) and Cr (30 %). The secondary peaks in NaF exposure were also investigated more closely since they were verging both Cr_2NiO_4 and Fe_2NiO_4. The experimental data was closer to Cr_2NiO_4, however, the peaks in Fig. 6a are broad and they can be a mixture of both Fe_2NiO_4 and Cr_2NiO_4. Considering that the alloy is richer in Cr than Fe, it is convincing that the Cr richer oxide is more detectable. As can be seen in Fig. 6a, sodium was never detected as part of the compounds in the oxide scale in NaF exposures. Also, in EDX results in 3 and 4, sodium and fluoride were always overlapping each other, meaning that they never got engaged in separate compounds. The Mo rich layer mentioned in EDX results in Fig. 5, which overlapped with the fluoride lean layer matched with the XRD pattern for $MoO_{2.8}F_{0.2}$. Since the corrosion layer was at least 120 μm thick in case of NaF exposures, all the less intense signals for $MoO_{2.8}F_{0.2}$ were not detected.

Table 3)
Main and secondary peaks in XRD analysis in NaF exposures and the corresponding compounds

oxide	2q	intensity	reference
NiO	43.286	100	[30]
	37.255	63.2	
	62.87	54.1	
$Cr_{0.3}Ni_{0.7}O_{0.65}$	43.53	100	[31], ICDD pdf 5
	37.46	97.16	
	63.26	54.81	
Experimental data from NaF exposures	43.56	100	
	37.5	43.71	
	63.24	67.25	
$NiFe_2O_4$	35.96	100	[32]
	63.54	44.26	
	57.85	31.22	
	30.53	30.57	
$NiCr_2O_4$	35.78	100	[33]
	63.19	34.1	
	30.37	32.4	
	57.54	28.3	
Experimental data for secondary peaks from NaF exposures	35.62	6.16	
	36.14	9.59	
	57.86	5.28	
	58.00	5.24	
	57.44	4.71	
	30.60	4.11	
	30.66	4.17	

XRD results for LiF exposures in Fig. 6b, showed peaks for both the oxide and the underlying metal which was depleted in Cr, Nb and Fe. After 1000 h, MoNi were detected as the base metal, since other alloying elements had reacted to oxygen. LiF was also detected since the sample was not washed after exposure.

Data Availability

Data will be made available on request.

References

[1] K. Sridharan, T. Allen, Corrosion in molten salts. in Molten salts chemistry, Elsevier, 2013, pp. 241–267.
[2] D. Williams, TN (United States). Assessment of candidate molten salt coolants for the NGNP/NHI heat-transfer loop, Oak Ridge National Lab.(ORNL), Oak Ridge, 2006.
[3] X.-X. Ye, et al., The high-temperature corrosion of Hastelloy N alloy (UNS N10003) in molten fluoride salts analysed by STXM, XAS, XRD, SEM, EPMA, TEM/EDS, Corros. Sci. 106 (2016) 249–259.
[4] M. Kondo, et al., Metallurgical study on corrosion of austenitic steels in molten salt LiF–BeF2 (Flibe), J. Nucl. Mater. 386 (2009) 685–688.
[5] A.K. Misra, J.D. Whittenberger, Fluoride salts and container materials for thermal energy storage applications in the temperature range 973–1400 K. in 22nd Intersociety Energy Conversion Engineering Conference, American Institute of Aeronautics and Astronautics, 1987.
[6] L.C. Olson, et al., Materials corrosion in molten LiF–NaF–KF salt, J. Fluor. Chem. 130 (1) (2009) 67–73.
[7] T. Liu, et al., Corrosion of alloys in high temperature molten-salt heat transfer fluids with air as the cover gas, Sol. Energy 191 (2019) 435–448.
[8] Y.L. Wang, et al., Effects of the oxidants H2O and CrF3 on the corrosion of pure metals in molten (Li, Na, K) F, Corros. Sci. 103 (2016) 268–282.
[9] M.S. Sohal, et al., Engineering database of liquid salt thermophysical and thermochemical properties, Idaho National Lab.(INL), Idaho Falls, ID (United States), 2010.
[10] Y. Wang, C. Zeng, W. Li, The influence of temperature gradient on the corrosion of materials in molten fluorides, Corros. Sci. 136 (2018) 180–187.
[11] R.H. Banerjee, et al., Investigating Cr dealloying and Li ingress in Ni-Mo-Cr alloys with different Mo/Cr ratio exposed to FLiNaK salt, Corros. Sci. 212 (2023) 110929.
[12] R.H. Banerjee, et al., A comparative study of surface layer formation in Ni-based alloys with varying Cr contents exposed to high temperature fluoride environment, J. Nucl. Mater. 516 (2019) 54–62.
[13] G.K. Johnson, The enthalpy of formation of FeF3 by fluorine bomb calorimetry, J. Chem. Thermodyn. 13 (5) (1981) 465–469.
[14] H. Zhou, et al., Controlled formation of mixed nanoscale domains of high capacity Fe2O3–FeF3 conversion compounds by direct fluorination, ACS nano 9 (3) (2015) 2530–2539.
[15] J.-E. Eriksson, et al., The effect of Cl, Br, and F on high-temperature corrosion of heat-transfer alloys, Fuel 348 (2023) 128516.
[16] H. Wu, P. Yrjas, M. Hupa, Laboratory studies of potassium-halide-induced high-temperature corrosion of superheater steels. Part 1: exposures in dry air, Energy Fuels 29 (2) (2015) 1186–1195.
[17] H. Grabke, E. Reese, M. Spiegel, The effects of chlorides, hydrogen chloride, and sulfur dioxide in the oxidation of steels below deposits, Corros. Sci. 37 (7) (1995) 1023–1043.
[18] H. Asteman, M. Spiegel, Investigation of the HCl (g) attack on pre-oxidized pure Fe, Cr, Ni and commercial 304 steel at 400C, Corros. Sci. 49 (9) (2007) 3626–3637.
[19] S. Enestam, et al., Are NaCl and KCl equally corrosive on superheater materials of steam boilers? Fuel 104 (2013) 294–306.
[20] F. Mansfeld, N. Paton, W. Robertson, The high temperature behavior of superalloys exposed to sodium chloride: II. corrosion, Metall. Trans. 4 (1973) 321–327.

[21] Ozeryanaya, I., Corrosion of metals by molten salts in heat-treatment processes. Met. Sci. Heat Treat. Met.(Engl. Transl.);(United States), 1985. **27**(3).
[22] M. Kondo, et al., Corrosion characteristics of reduced activation ferritic steel, JLF-1 (8.92 Cr–2W) in molten salts Flibe and Flinak, Fusion Eng. Des. 84 (7-11) (2009) 1081–1085.
[23] R.N. Sodhi, Time-of-flight secondary ion mass spectrometry (TOF-SIMS):—versatility in chemical and imaging surface analysis, Analyst 129 (6) (2004) 483–487.
[24] A. Nikbakht, B. Bahramian, C. Geers, Deep intergranular fluoride attack by high-temperature corrosion on alloy 625 by LiF in air at 600° C, High. Temp. Corros. Mater. 101 (5) (2024) 1055–1066.
[25] E. Sullivan, et al., Structure, stability, and photoluminescence in the anti-perovskites Na3W1− xMoxO4F (0≤ x≤ 1), J. Solid State Chem. 230 (2015) 279–286.
[26] Y. Asakura, et al., Synthesis of NaMoO3F and Na5W3O9F5 with morphological controllability in non-aqueous solvents, Inorg. Chem. 59 (15) (2020) 10707–10716.
[27] C.W. Bale, et al., FactSage thermochemical software and databases, Calphad 26 (2) (2002) 189–228.
[28] M. Spiegel, Salt melt induced corrosion of metallic materials in waste incineration plants, Mater. Corros. 50 (7) (1999) 373–393.
[29] G. Villalba, R.U. Ayres, H. Schroder, Accounting for fluorine: production, use, and loss, J. Ind. Ecol. 11 (1) (2007) 85–101.
[30] H.E. Swanson, Standard X-ray diffraction powder patterns, 25, US Department of Commerce, National Bureau of Standards, 1953.
[31] E.E. Sileo, et al., Thermal decomposition of Crystalline NiII− CrIII layered double hydroxide: a structural study of the segregation process, J. Phys. Chem. B 109 (20) (2005) 10137–10141.
[32] T. Tangcharoen, A. Ruangphanit, W. Pecharapa, Structural and magnetic properties of nanocrystalline zinc-doped metal ferrites (metal= Ni; Mn; Cu) prepared by sol–gel combustion method, Ceram. Int. 39 (2013) S239–S243.
[33] E. Verwey, E. Heilmann, Physical properties and cation arrangement of oxides with spinel structures I. Cation arrangement in spinels, J. Chem. Phys. 15 (4) (1947) 174–180.